

Velocities in the plume of the 2010 Eyjafjallajökull eruption

H. Bjornsson,¹ S. Magnusson,² P. Arason,¹ and G. N. Petersen¹

Received 24 May 2013; revised 6 September 2013; accepted 30 September 2013; published 22 October 2013.

[1] The eruption of the Icelandic volcano Eyjafjallajökull in the spring of 2010 lasted for 39 days with an explosive phase (14–18 April), an effusive phase (18 April to 4 May) and a phase with renewed explosive activity (5–17 May). Images every 5 s from a camera mounted 34 km from the volcano are available for most of the eruption. Applying the maximum cross-correlation method (MCC) on these images, the velocity structure of the eruption cloud has been mapped in detail for four time intervals covering the three phases of the eruption. The results show that on average there are updrafts in one part of the cloud and lateral motion or downdrafts in another. Even within the updraft part, there are alternating motions of strong updrafts, weak updrafts, and downward motion. These results show a highly variable plume driven by intermittent explosions. The results are discussed in the context of integral plume models and in terms of elementary parcel theory.

Citation: Bjornsson, H., S. Magnusson, P. Arason, and G. N. Petersen (2013), Velocities in the plume of the 2010 Eyjafjallajökull eruption, *J. Geophys. Res. Atmos.*, 118, 11,698–11,711, doi:10.1002/jgrd.50876.

1. Introduction

[2] A volcanic plume rising into the atmosphere is a spectacular, awe inspiring phenomenon. The rising plume is a turbulent mixture of volcanic ash, gases, entrained atmospheric water, and air. In the standard conceptual model of a volcanic plume [Sparks *et al.*, 1997], a plume can be split into three regions or dynamic phases: Just above the vent, the plume is a high-velocity mixture of gas and solids that rises on account of its own momentum. In this phase the plume is denser than the ambient air, but as it rises, its density is reduced through the entrainment, mixing, and heating of ambient air. If this process continues for a sufficient length of time, it will make the plume positively buoyant and from which point it rises convectively. The transition from the gas thrust phase to the positively buoyant convective phase can occur few hundred meters to a few kilometers above the vent [Sparks, 1986], depending on the eruption strength. The convective phase typically makes up the majority of the vertical extent of the plume; for intermediate and weak eruptions, it reaches a few kilometers in altitude, but for strong eruptions, it can reach into the stratosphere. Eventually, the rising plume loses its buoyancy and as it approaches its level of neutral buoyancy it enters the third and topmost region, the umbrella, where it spreads out and ash may be advected into the far field.

[3] Although the description above, strictly speaking, only applies to Plinian eruptions, salient features of it can apply to other types of eruptions. For instance, associated with a nonexplosive effusive eruption, the lava may act as an intense heat source leading to the formation of a buoyant cloud. Indeed, theoretical understanding of the dynamics of volcanic plumes originates in work on the dynamics of thermally buoyant plumes [Morton *et al.*, 1956]. One aspect of the theory is that subject to certain assumptions about the dynamics, a scaling rule can be derived relating the height of a steady thermal plume to the one-fourth power of the strength of the heat source. For purely thermal plumes this scaling rule is backed up with empirical evidence [Morton *et al.*, 1956; Briggs, 1969; Carazzo *et al.*, 2008], but remarkably, it has also been found to apply to volcanic plumes, although with a slightly different exponent [Carey and Sparks, 1986; Mastin *et al.*, 2009]. That such a scaling rule should apply to volcanic plumes is not obvious, since during volcanic eruptions the height of the plume is potentially also affected by factors such as the extent of the gas thrust region, ash loading and fallout, the atmospheric temperature lapse rate [Glaze and Baloga, 1996], humidity [Tupper *et al.*, 2009], variable entrainment rate of ambient air; which can be affected by wind [Bursik, 2001] and/or atmospheric stratification [Carazzo *et al.*, 2008]. Recent modifications of this scaling rule, incorporating the effects of wind shear [Woodhouse *et al.*, 2013] and extending it to plumes bent over by the wind [Degruyter and Bonadonna, 2012] have further cemented its application to volcanic eruptions.

[4] Expanding on Morton *et al.* [1956] and other previous work [Wilson, 1976; Wilson *et al.*, 1978; Settle, 1978; Sparks and Wilson, 1982; Sparks, 1986; Wilson *et al.*, 1987], Woods [1988] published a model combining the three distinct regions of volcanic plumes. As well as predicting the

Additional supporting information may be found in the online version of this article.

¹Icelandic Meteorological Office, Reykjavik, Iceland.

²Division of Optimization and Systems Theory, Royal Institute of Technology, Stockholm, Sweden.

Corresponding author: H. Bjornsson, Icelandic Meteorological Office, Bustadavegur 9, IS-150 Reykjavik, Iceland. (halldor@vedur.is)

height of the plume, this model also predicted the average velocity profile in the plume depending on source-related parameters, such as amount of solid pyroclasts, vent diameter, velocity, and plume temperature at the source. Subsequent modeling work added the influence of ambient wind [Bursik, 2001; Woodhouse *et al.*, 2013] and improved the thermodynamics of the plume [Mastin, 2007]. For the steady state conditions, assumed in the above models to apply, the steady source must be maintained for a duration of time significantly longer than the ascent time of the plume. In cases where this does not apply, the time-dependent version of thermal plume theory [Scase *et al.*, 2006], as applied to volcanic eruptions by Scase [2009], is needed.

[5] The above models are integral models, in that the plume is at each height-level treated as well mixed and thus its temperature, velocity, density, etc. can be represented by a profile reflecting the average conditions at each altitude. Even in the case of time-dependent models, it is assumed that the turbulent motion in the plume mixes its constituents fast enough for these average profiles to be meaningful and representative.

[6] The decrease in velocity that occurs in the gas thrust phase may continue, albeit at a slower rate in the convective phase. For strong enough eruptions, models can also show super-buoyant behavior [Bursik and Woods, 1991], where the plume velocities increase after the transition to a buoyant phase. However, the observational evidence for these velocity profiles is not extensive; a short summary is given below.

[7] One of the first studies of velocities in a volcanic plume was that of Sigurgeirsson [1966], who analyzed camera data from 1 Dec 1963 to estimate velocities of individual cloud turrets in the upper part of the plume during the Surtsey eruption. The velocities ranged from 10 to 14 m s^{-1} at 6 to 8 km altitude. While not explicitly stated, it is likely that the cloud turrets originated in explosions at the vent, but Sigurgeirsson [1966] reports them as rising faster than surrounding plume to an altitude of about 8 km.

[8] Early observations of velocities in volcanic plumes, summarized in Sparks *et al.* [1997], were focused on starting plumes, the initial thermal that rises from a maintained source. Analysis of the 22 April 1979 eruption of the Soufriere, St. Vincent volcano, showed that in the first 3 min, the plume rose almost 9 km, but it was fed by a sequence of starting plumes, resulting from closely spaced (in time) explosions at the vent. These starting plumes had velocities ranging from 8.5 m s^{-1} to 62 m s^{-1} , with stronger plumes overtaking earlier weaker plumes. Similarly, during the initial phase of the 20 Feb 1990 Lascar eruption, two starting plumes with different velocities were analyzed. For the weaker one, the vertical velocity of the leading edge was about 30 m s^{-1} at 2 km above the vent, but had reduced to about 10 m s^{-1} at 8 km. The stronger plume had velocities of about 55 m s^{-1} at 4 km above the vent, falling to about 10 m s^{-1} at 14 km. A velocity profile calculated from data collected on the 17 October 1980 during the Mount St. Helens eruption showed velocities falling from an initial value of about 50 m s^{-1} at 600 m above the vent to just over 20 m s^{-1} at 800 m height, increasing to 40 m s^{-1} in the next 80 m of ascent.

[9] Sparks *et al.* [1997] also summarized observations of velocities in the gas thrust phase from the Heimae 1973

eruption. Estimates of the gas motion were based on tracking of particles that were small enough to be considered embedded in the gas flow. The analysis revealed velocities in the 150–200 m s^{-1} range about 50 m above the volcano, decelerating rapidly in the next 50–100 m and then reaching steady values of 25–35 m s^{-1} about 150 m above the vent. More recent observations from Stromboli using high frame rate thermal cameras have revealed a high velocity gas jet just above the vent, that could carry small particles at an average velocity of about 80 m s^{-1} , but with the gas jet reaching velocities of 213 m s^{-1} [Harris *et al.*, 2012]. In another study, using a high frame rate thermal camera, the velocities at the Santiaguito volcano were estimated to range from 15 to 50 m s^{-1} within the gas thrust region, but 4–15 m s^{-1} above that [Sahetapy-Engel and Harris, 2009].

[10] Petersen *et al.* [2012] analyzed camera data from the 2010 Eyjafjallajökull eruption and estimated starting plume ascent velocities for three different periods of the eruption. This eruption had an explosive phase (14–18 April), an effusive phase (18 April to 4 May) and phase with renewed explosive activity (5–17 May) [Gudmundsson *et al.*, 2012]. The results show that during the weak effusive phase, velocities ranged from about 20 m s^{-1} just above the vent but fell to zero within a kilometer above the vent. During the explosive phases, the height of the plume varied. When the eruption was at its strongest, and the plume rose above 5 km altitude, velocities ranged from 15 to 30 m s^{-1} in the convective part of the plume, but during a time when the plume only rose to about 4 km altitude, the velocities ranged from 15 m s^{-1} in the lower part of the plume to 5 m s^{-1} in the upper part.

[11] The above summary of volcanic plume velocity estimates supports higher velocities in gas thrust phase than in the convective phase, but also shows how convective phase velocities can vary within the same eruption, when the plume is supported by a sequence of discrete explosions at the vent. As is to be expected, there is also a big difference between eruptions of different types and strength.

[12] However, it should be noted that the above studies do not provide detailed empirical evidence for the velocity profiles predicted by the integral models. Indeed the structure of the velocity field within an eruption plume, its spatial and temporal variability, has not been described in any detail. It is possible that the observed starting plume velocities discussed above are not reflective of average plume velocities, in which case these observations would have little bearing on profiles predicted by the models. In this regard, several questions need to be considered: (a) What is the average velocity within an eruption cloud? (b) What is its temporal and spatial variability?—And related to these, (c) how well do the velocities of discrete plumes, arising from an explosion at the vent, reflect the average velocities within the cloud?

[13] The purpose of this paper is to examine these questions using data from the 2010 Eyjafjallajökull eruption. In section 2 we describe the data used and section 3 contains a description of the methods. Results of the analysis are given in section 4. In this section we begin by examining the velocities of identifiable features in the eruption plume. Typically, these features are cloud turrets that originate in an explosion at the vent, and might thus be considered as analogous to the starting plumes discussed above. Next, we examine the plume velocity field, its average spatial structure, and its temporal variability. We then examine the average profile

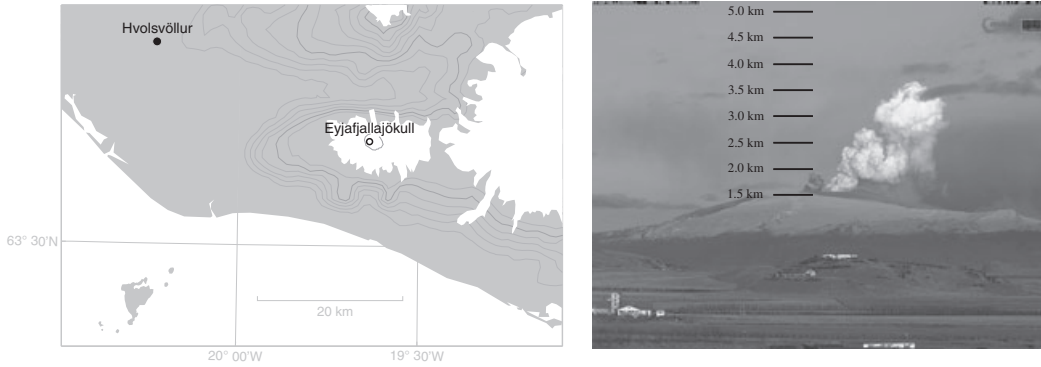


Figure 1. (left) Map showing the location of the camera in Hvolsvöllur and the summit eruption vent. (right) An example of an image from the camera at Hvolsvöllur. The photo is taken at 20:12:14 UTC on 17 April. An approximate height scale valid above the vent (km asl) has been added to the photo.

of vertical velocity and contrast that with the turret velocities derived earlier. Finally, we study how representative the average velocities are by examining a 6 h segment from 17 April. We conclude with a discussion section.

2. Data

[14] Several cameras were mounted with a view of the Eyjafjallajökull volcano in April to May 2010. The most useful camera for monitoring the height evolution of the plume was located in the village of Hvolsvöllur, 34 km from the volcano. It had a clear view of the volcano and the sky above up to about 5.2 km above sea level (asl) (Figure 1). The camera images were saved every 5 s, with vertical resolution at the volcano of about 15 pixels per 100 m. During a few days in May, the camera was switched to a low resolution mode with only about 9 pixels per 100 m. While the duration of the eruption was 39 days, the camera only afforded a clear view of the entire plume for a few of these days, due to low-visibility weather such as low clouds, precipitation, night-time darkness, mist or haze. On an hourly basis, there was a clear view of the plume-top 17% of the time. *Arason et al.* [2011] describe the camera data and its limitations in more detail. In the present study, the data is limited to 3 days, one from each phase of the eruption. The first day is 17 April, when the eruption was explosive and visibility was very good. On 20 April, the second day analyzed here, the eruption had entered the effusive phase and explosive activity had ceased. On 11 May, the third day analyzed here, explosive activity had started again. However, by this time, prevalent haze meant that visibility was worse than during the two other days analyzed, and furthermore on this day, the camera had been switched to the low resolution mode. While this results in noisier images on 11 May than during the earlier days, the images are still of sufficient quality to yield useful information on the velocities in the plume.

[15] Based on comparison of weather radar data and plume top height altitudes derived from these images, *Arason et al.* [2011] estimated that for the duration of the eruption, crosswind effects result in an uncertainty in plume-top altitudes that are on the order of 10%. In this respect there are two issues related to the aspect of the plume, as seen from the cameras, that need to be discussed. First, the

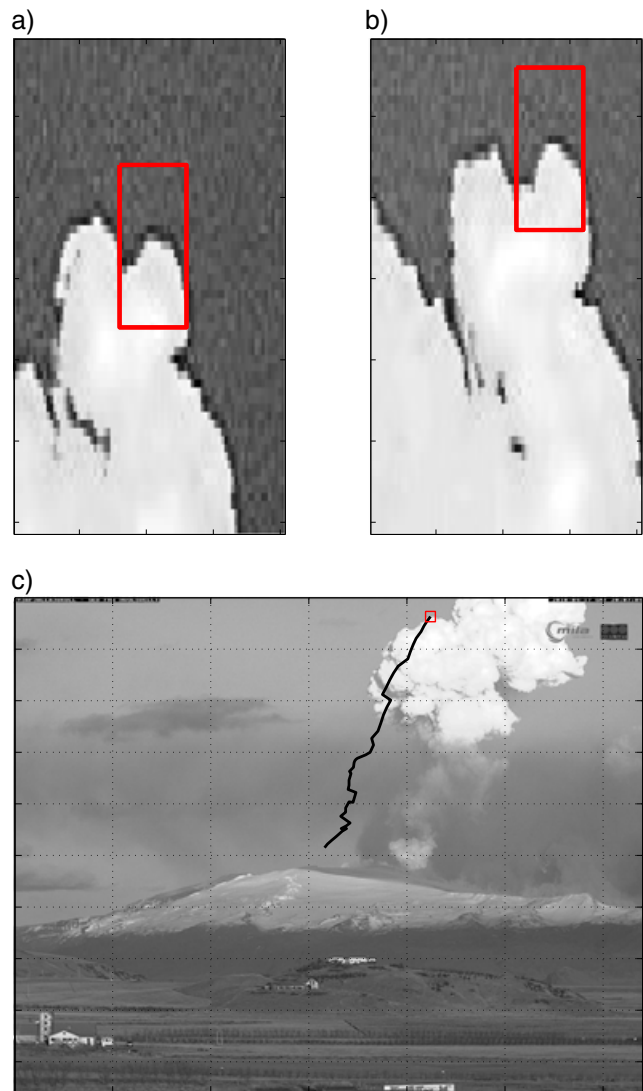


Figure 2. (a and b) An example of the tracing of an identifiable feature between successive images. In this case a turret in Figure 2a is traced to Figure 2b. (c) The result of tracking a feature throughout the ascent of the plume.

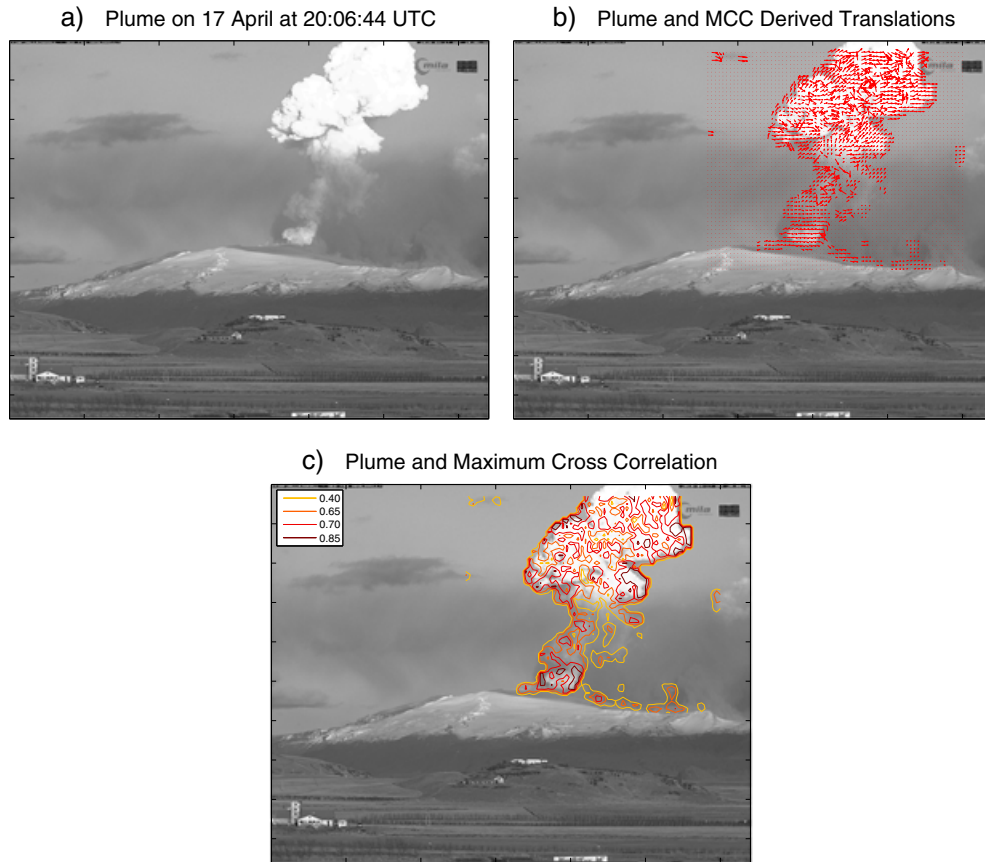


Figure 3. Instantaneous snapshot of the plume and its motion. (a) The eruption plume on 17 April at 20:06:44 UTC. (b) Translation vectors for each grid point where the MCC was higher than 0.4. The vectors show the direction that each point is translated to in the subsequent image. (c) The maximum cross correlation (MCC) for each point where MCC is higher than 0.4. The key to the contours is given in the legend.

winds can blow the plume away from (toward) the camera, in which case the scale in Figure 1 will underestimate (overestimate) the true altitude of the plume. The second issue relates to the fact that an expanding plume is a three-dimensional structure, so even without wind, the upper part of the plume, as seen from the cameras, would not be in the same vertical plane as the lower part of the plume. Below, these two issues are addressed in turn.

[16] As Figure 1 shows, the volcano lies to the ESE of the village Hvolsvöllur, so ideally the winds aloft should be from NNE for the eruption cloud to drift perpendicular to the line of sight. However, the actual winds deviated from this direction, and we have tried to examine the degree to which this affected our results.

[17] Using the model-derived wind field that was used to drive the UK Met Office's Numerical Atmospheric-dispersion Modeling Environment (NAME) for the Eyjafjallajökull eruption [Dacre *et al.*, 2011], we examined the influence of the winds over Eyjafjallajökull on the plume motion estimates for the 3 days used here. We calculated the average winds in the layer 4 km above the volcano, and the angle with which the winds aloft deviated from the direction perpendicular to the line of sight. We found that, during the 17 April intervals, the wind direction aloft ranged from 17 to 21° away from this direction, with average velocities

of about 14 m s^{-1} ; on 20 April, the angle was 51° and the average wind about 12 m s^{-1} ; and on 11 May, the angle was 43° and the average wind about 18 m s^{-1} . Based on a visual examination of the image sequence, we found that the time that it took a cloud feature to rise from the vent to the top of the plume was generally less than 5 min, which means that it would at most drift from the vent by about 5 km. Based on these numbers, we calculated how the apparent height that a plume top at 4 km altitude but displaced 5 km away from the vent in the direction of the prevailing wind, would appear in our images. We found that in this case the apparent altitude as seen in our images would have been less than 6% below the true altitude on 17 April, but 10–11% on the other 2 days.

[18] The expansion of the plume into the atmosphere can lead to an overestimation of the true altitude of the plume, if the top of the plume is in a vertical plane that is closer to the camera than the vent is. However, if the sideways expansion of the plume is used as a guide, Figures 1–3 show that the plume width was at most 1–2 km, which means that the absolute error due to the expansion of the plume is much less than the error due to the wind. As the wind effects were actually leading to an underestimate of the true plume height, any expansion effect would act to reduce that underestimation.

[19] To summarize, the errors in estimating plume altitude due to the expansion of the plume and due to wind

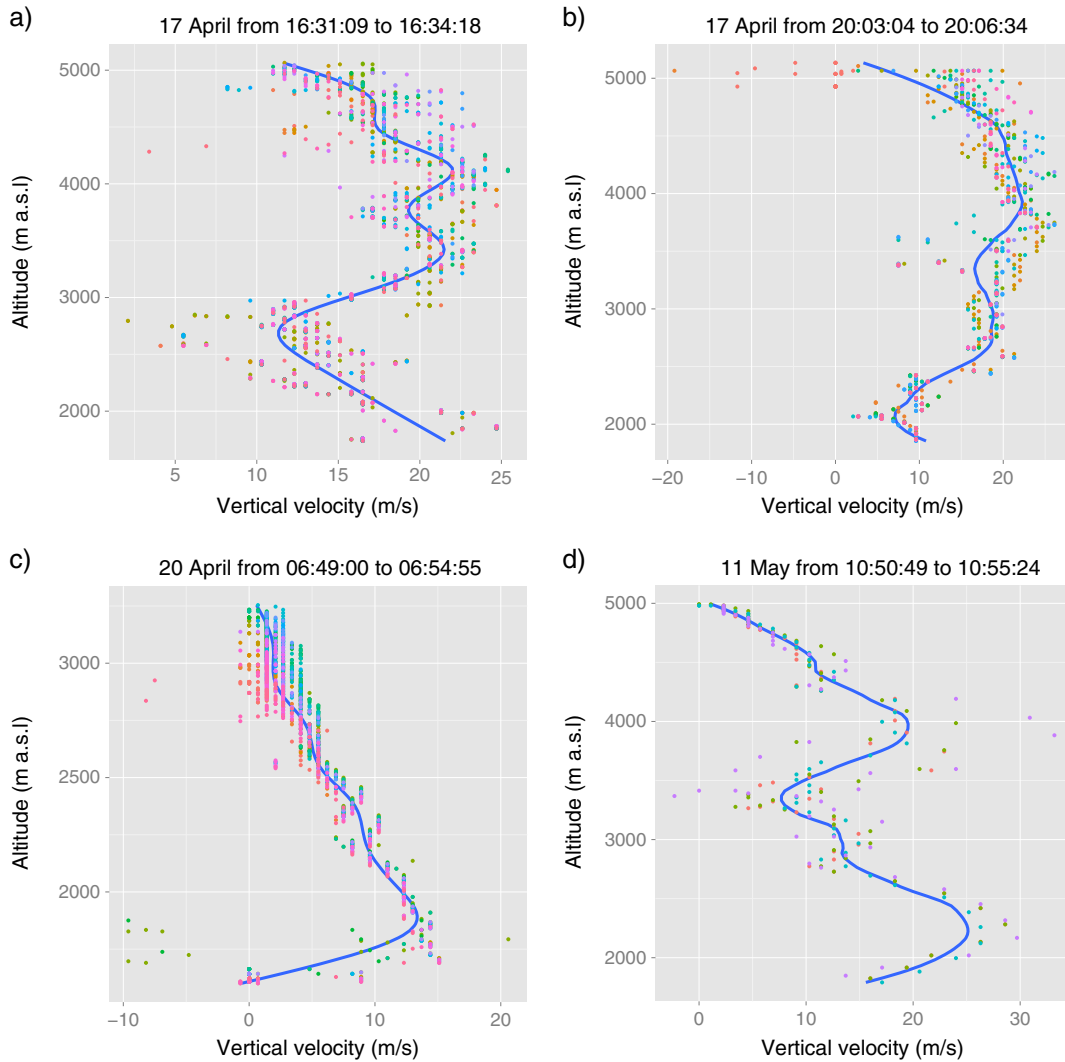


Figure 4. Velocity profiles obtained by Lagrangian tracing of identifiable features on the edge of the volcanic cloud. (a and b) Results from 17 April, when the eruption was explosive with ash fall at low levels from the cloud, (c) results from April 20, the effusive phase of the eruption, and (d) results from 11 May, during the second explosive phase. For each image the colored points indicate the identifiable feature being tracked and the number of features available for tracking varies between images. The solid line is a loess smoother line showing the average velocity by altitude.

drift are at most just above 10%, in agreement with the estimates of *Arason et al.* [2011]. Since the camera clock did not drift, these are the same percentage errors we get in our velocity estimates.

3. Methods

[20] Automated methods for cloud tracking have a long history in the meteorological community [*Clark et al.*, 1968; *Leese et al.*, 1971; *Arking et al.*, 1978]. Different classes of algorithms exist for tracking apparent motion in satellite images (see discussion in *Velden et al.* [2005] for details). Among the simpler methods is the maximum cross-correlation (MCC) method that searches for the highest correlation between small blocks of pixels in sequential images. This method has applications in different geoscience-related fields [*Laverne et al.*, 2010; *Yahia et al.*, 2010] and is

widely used to estimate atmospheric motion vectors [*Giri and Sharma*, 2011]. Two variants of the MCC method have been developed here. Both methods work on a sequence of images, consisting of several minutes of images taken every 5 s.

[21] In the first one, an identifiable feature is selected, typically, a part of a cloud turret that is rising following an explosion at the vent. A box encompassing the feature is defined, and in the next image in the sequence, the box that has the highest correlation with the first box is found (Figures 2a and 2b). Proceeding this way through the whole sequence of images allows us to track the motion of the feature (Figure 2c). While the method is not sensitive to slow changes in the shape of the feature being tracked, it can fail if the feature changes rapidly. Likewise, the method may be distracted by other motion, such as horizontal cloud motion in the background of the images. Such failures are

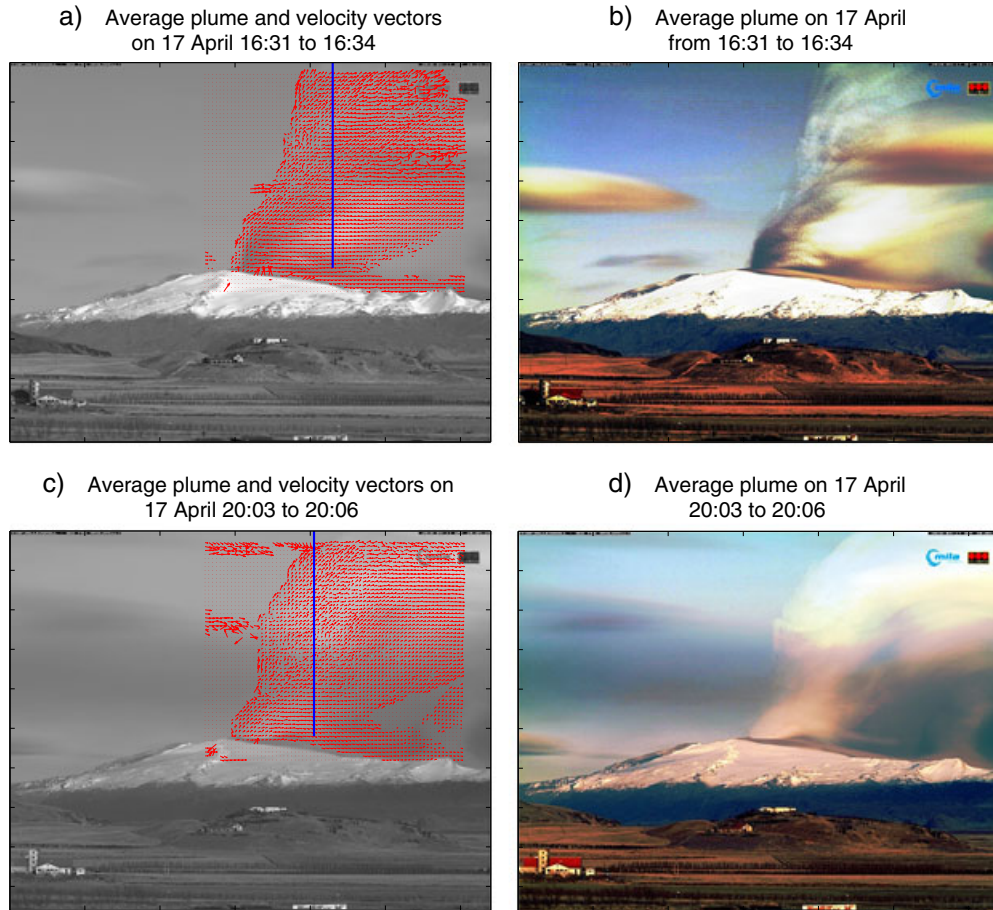


Figure 5. Average plumes and average motion in the plume on 17 April for the periods (a and b) 16:31–16:34 UTC and (c and d) 20:03–20:07. The color in images 5b and 5d has been adjusted to enhance the plume visibility, and average motion vectors in Figures 5a and 5c were only calculated for cases where $MCC > 0.4$.

easy to spot by visual inspection of the tracks obtained (see Figure 2c). Once the tracks are obtained, the vertical velocity is found by differentiation. Details on the algorithm can be found in Appendix A and in programs in the supporting information.

[22] This method attempts a *Lagrangian* tracking of a cloud feature. While the track allows us to estimate the ascent velocity of the feature tracked, it provides incomplete information on the velocities within the plume. Obviously, the method can only see motion on the exterior of the plume; any velocity structure within the cloud that does not have an expression on the exterior will remain unknown. Furthermore, the velocities obtained are not uniformly distributed on the outside of the plume. The second issue can be resolved using another variant of the MCC method to estimate motion throughout the exterior of the plume. In this case the plume (Figure 3a) is overlaid with a grid, a box defined around each grid point, and in the next image, the MCC method is used to find the box that is the closest representation of the first box. As this calculation was done for each point on the grid, it yields an estimate of how all parts of the plume seen from the camera were translated between images. This was done for the whole sequence of images, and from this the velocities on the exterior of the cloud could be mapped (Figure 3b).

[23] The main difference between these methods is that the first one tracks a specific feature, whereas the second method attempts to give a snapshot of the motion for successive images and hence the velocities. An estimate of the average velocity can then be obtained by averaging the entire sequence of images. As this second method estimates velocities on a grid, it can be thought of as giving velocities in an *Eulerian* framework. (This labeling of the methods is for convenience and should not be taken too literally).

[24] For successive images this Eulerian procedure gives information on the horizontal and vertical motions on the exterior of the plume, and also the value of the maximum cross correlation (MCC) at each point (Figure 3c). The MCC is an indicator of the quality of the reconstructions of plume motion, and can be used to screen out unreliable estimates. This can be seen in Figure 3c where MCC values within the plume exceed 0.4.

4. Results

4.1. Lagrangian Velocities

[25] Figure 4 shows the results obtained using the Lagrangian tracking method for four intervals during the eruption. Two of the intervals selected are from 17 April (from 16:31 to 16:34 UTC and from 20:03 to 20:06 UTC,

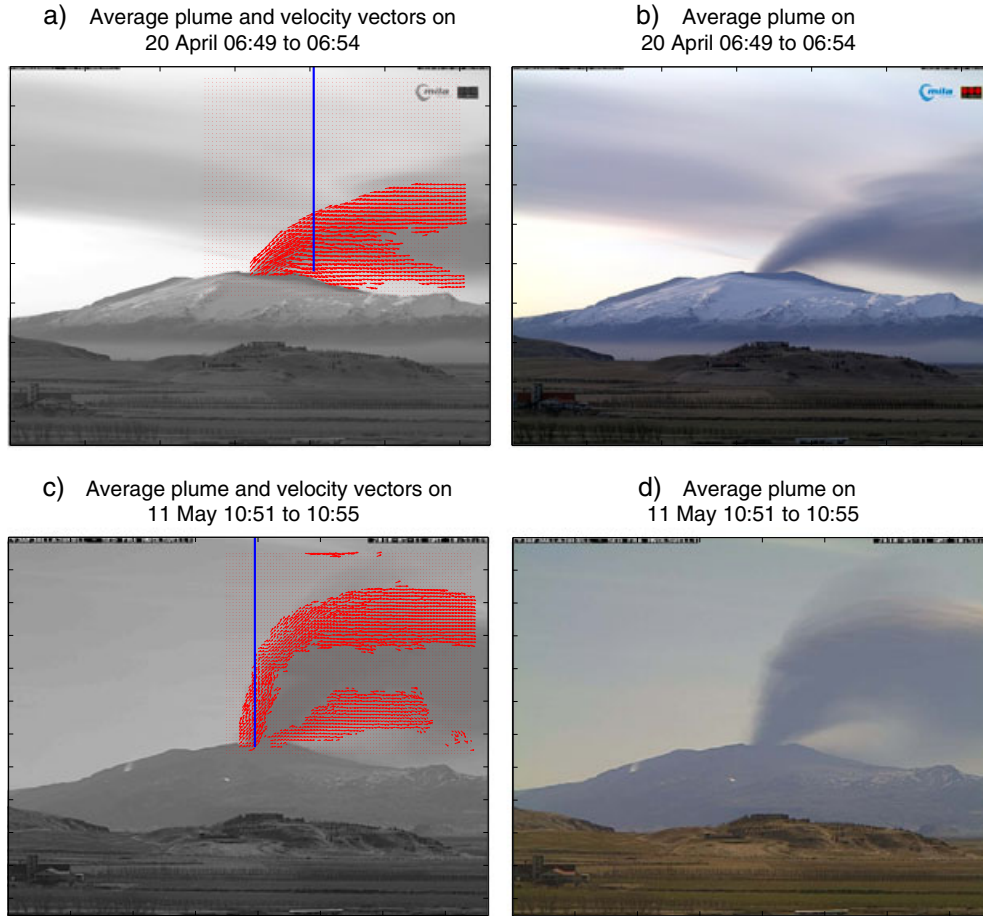


Figure 6. Average plumes and average motion in the plume on 20 April from (a and b) 06:49 to 06:54 UTC and (c and d) 11 May 10:51 to 10:55 UTC. The color in Figure 6c was adjusted to enhance the visibility of the plume. The average motion vectors in Figure 6a were only calculated for cases where $MCC > 0.4$, but in Figure 6c, the MCC limit was 0.5, and furthermore, the calculation in Figure 6c was restricted to points where the MCC exceeded 0.5 for more than 40% of the time interval.

respectively), one interval is from 20 April (from 06:49 to 06:55 UTC) and one is from 11 May (from 10:51 to 10:55 UTC). In each case, several identifiable features were examined, resulting in several tracks for each interval. Based on the tracks, the velocity as a function of altitude was calculated. In each panel, points of the same color belong to the same track, and the number of colors in each panel indicates the number of features tracked. The number of features varied, depending on visibility, the cloud structure, and its evolution at each interval. As each image from the camera is broken into a finite number of pixels, a feature can only travel an integer number of pixels during each 5 s interval, resulting in a discretization of the velocity estimates, which is apparent from the points lining up vertically in each of the panels. The solid line in each panel is a smooth loess curve through the average velocity at each level.

[26] Figures 4a and 4b show results obtained during the first explosive phase of the eruption, on 17 April. Both figures show an initial drop in velocity followed by a general increase with maximum values obtained near 4000 m altitude (~ 2300 m above the vent, which is at 1670 m altitude). Above this level, the rise of the features being tracked slows down, but in both cases the features eventually rise out of

the image frame (at 5200 m altitude). In both figures velocities in the upper part of the plume range from 15 to 25 m s^{-1} with the average around 20 m s^{-1} .

[27] Figure 4c is from 20 April when the eruption was effusive with little explosive activity. In this case the velocity estimates in the lowest 250 m of the plume are widely scattered but maximum velocities of about 15 m s^{-1} occur at around 1900 m altitude. From there the velocities drop, and between 3000 and 3500 m altitude the features being tracked have ceased rising.

[28] Figure 4d is from 11 May when explosive activity of the eruption had reinvigorated. As mentioned earlier, during the second explosive phase, visibility was reduced due to haze and thus fewer identifiable features could be tracked. Velocities in the lower part of the plume were quite high, with an average of 25 m s^{-1} in between 2000 and 2500 m altitude. Above this level the velocities fall to about 10 m s^{-1} at 3000 to 3500 m altitude, but then speed up and are about 20 m s^{-1} at 4000 m altitude, from where they decrease with altitude and are close to zero at 5000 m altitude.

4.2. Eulerian Velocities

[29] As noted above, many of the identifiable features lie on the leading edge of the rising plume. Most of them remain

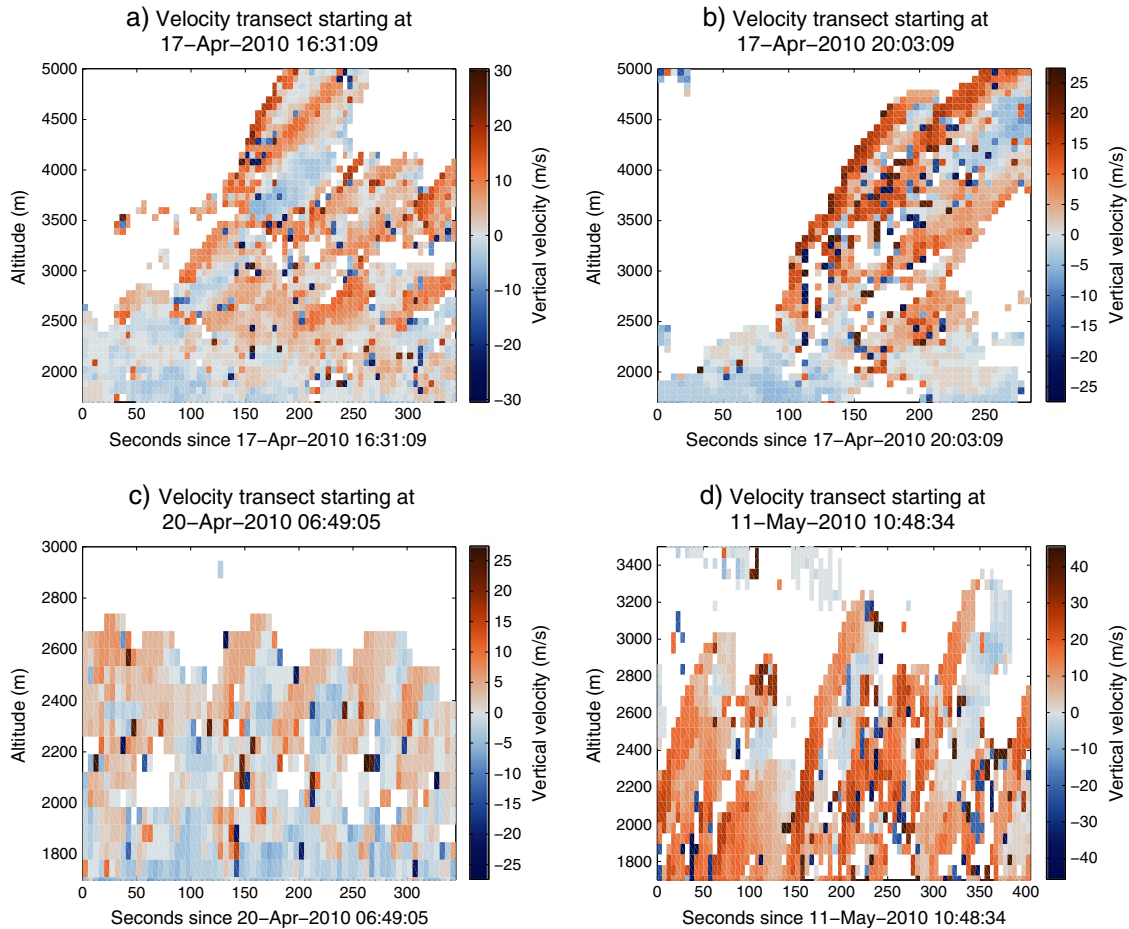


Figure 7. The temporal evolution of vertical velocity on a transect in the plume. The location of the transect is shown as a vertical line in Figures 5a, 5c, 6a, and 6c.

on the leading edge as they rise. Other turrets do, however, become embedded in the plume as they rise. As a consequence, the velocities in Figure 4 need not reflect average vertical velocities on the exterior of the cloud during the time intervals of the tracking. To estimate average velocity profiles, first, the average of the snapshots (as in Figure 3b) were calculated for each time interval.

[30] Figures 5 and 6 show the average motion vectors calculated for respective time intervals. Figures 5a and 5c show the average motion for the two intervals on 17 April superimposed on the average eruption cloud for each interval (Figures 5b and 5d). Examination of the estimated motion vectors shows rising motions on upwind side of the eruption cloud (above the vent), but lateral motion predominates on the downwind side (to the left of the vent). At low levels on the downwind side, the plume motion is oriented downward along the slope of the mountain. This is associated with suspended ash motion in the boundary layer, but during this phase of the eruption, there was substantial fallout [Gudmundsson *et al.*, 2012].

[31] Figure 6a shows the average motion for 20 April. In this case the plume is much weaker and bent over by the wind. Rising motion is apparent on the upwind side of the cloud, but lateral motion takes over at lower altitudes than on 17 April when the eruption was stronger. This can also be seen in Figure 6b, which shows the average cloud for the period as a bent over dispersive plume.

[32] Figures 6c and 6d show the results for 11 May. At this time the plume was clearly stronger than on 20 April, consistent with renewed explosive activity. However, as Figure 6c shows, visibility was reduced, resulting in velocities only being estimated on the edges of the plume; the middle of the plume was too featureless for the MCC method to work. As a consequence, velocity estimates were only obtained for the “lower” and “upward” part of the plume, where “upward” represents an area that extends from the vent to the upper part of the plume.

[33] The results shown in Figures 5a and 5c are only based on velocity estimates where the MCC was 0.4 or higher. While this was adequate, it should be noted that in Figure 5c, there are areas where background cloud motion confuses the MCC method. This can be seen as motion vectors that clearly lie outside the main plume. As such artifacts tend to arise from sporadic identification of motion outside the plume, they can be screened out by demanding that the MCC be higher than a threshold value for more than a certain percentage of the time interval studied. Figure 6 shows results where the average is only based on those points where the MCC exceeded a threshold value for at least 40% of the time interval. For 20 April (Figure 6a), the threshold value was 0.4, the same as in Figure 5, but for 11 May (Figure 6c) the MCC threshold for motion vector calculations was set to 0.5 due to the increased noise. This added constraint was sufficient to screen out noisier background motion.

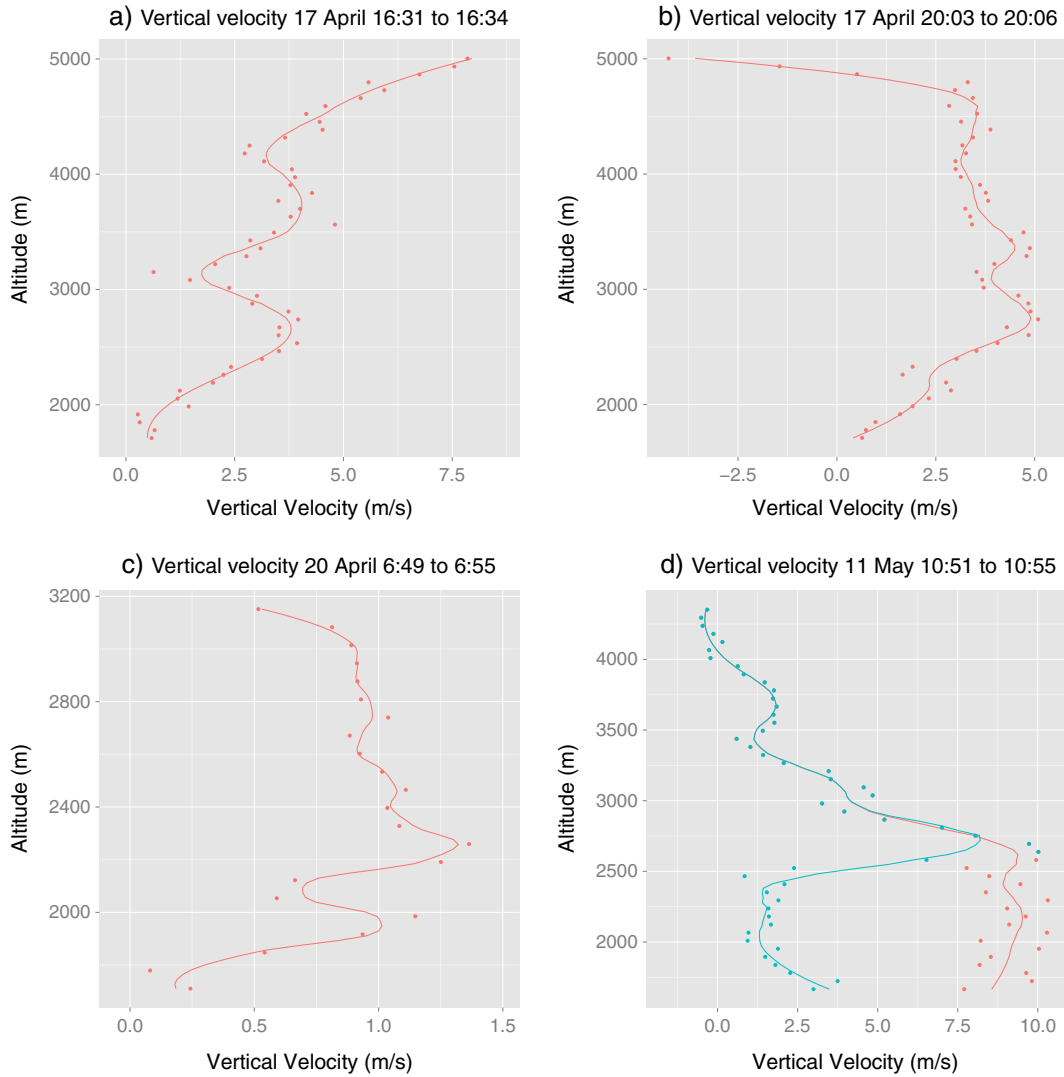


Figure 8. Velocity profiles calculated from plume motion vectors in Figures 5a, 5c, 6a, and 6c. The solid line shows a loess smoothing filter applied to the point values. In all figures the average profile is calculated from all motion estimates at a given level, except in Figure 8d, where additionally the red points and curve show the results from an average over only the upwind part of the plume.

[34] Figures 5 and 6 show the average spatial variability in the plume motion. In general there are updrafts in large parts of the plume, downwind from the vent lateral motion prevails, and even downward motion at lower levels. However, the average motion in the figures masks a significant amount of temporal variability as can be seen in Figure 7, which shows the time behavior of vertical velocity on transects defined by the vertical lines in Figures 5a, 5c, 6a, and 6c.

[35] Figure 7 shows the pulsating nature of the plume motion, with several intervals of high vertical velocity on each panel. This is very clear for the days when the eruption was in an explosive phase (Figures 7a, 7b, and 7d) but even in the weak plume case of 20 April (Figure 7c), the plume can be seen pulsating although the velocities are lower. The high-velocity pulses can be associated with features like the turrets examined with the Lagrangian method. They can be seen rising with a velocity far in excess of the background motion. Indeed, the vertical velocities following

the passing of a turret can even be negative. A good example of this can be seen in Figure 7a where velocities above 10 m s^{-1} are seen about 100 s into the sequence at around 2700 m altitude. This high velocity feature then rises in the next 100 s to 5000 m altitude. Immediately below this feature, the velocity is lower, or about $0\text{--}5 \text{ m s}^{-1}$, and below that the vertical velocity is negative. These alterations in vertical velocity are not surprising if the turrets are behaving as ring vortices [Turner, 1973], characteristic of rising thermals in atmospheric convection clouds [Rogers and Yau, 1989]. In that case, downward motion below the thermals would be expected.

[36] It is noteworthy that velocity vectors in Figures 5 and 6 show that on average there are updrafts in one part of the eruption cloud and downdrafts in another part. Furthermore, Figure 7 shows alternating upward and downward motion within the updraft part of the cloud. Figure 8 show the average plume velocities, i.e., the velocity profiles obtained by spatially averaging the vertical component of the velocity

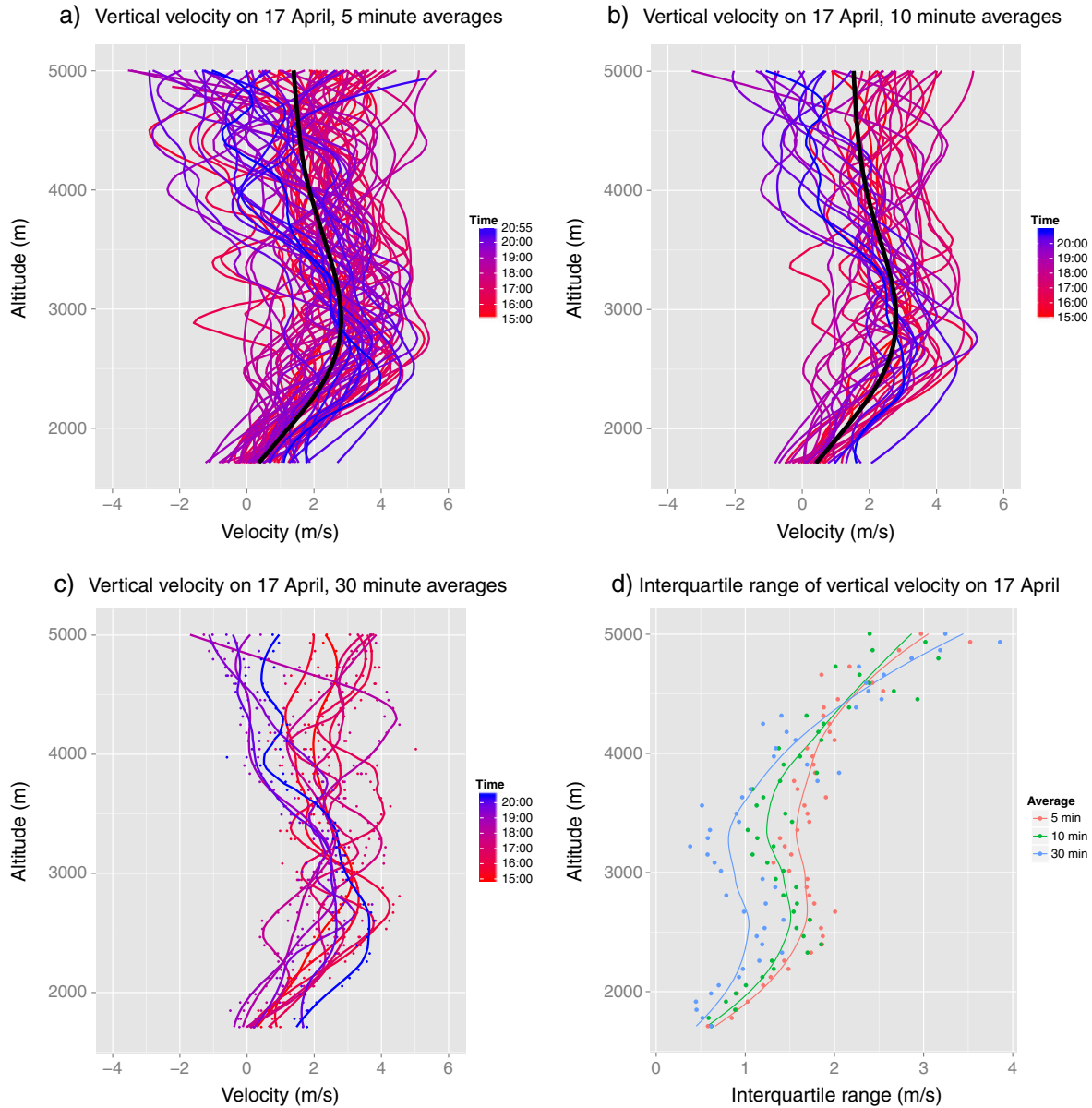


Figure 9. Velocity profiles on 17 April from 15:00 to 21:00 UTC. (a) All 5 min average profiles, (b) all 10 min averages, and (c) all 30 min averages. (d) The interquartile range of velocity estimates as a function of altitude for the different averaging periods. For visualization purposes in Figures 9a and 9b, only the smoothing filter (same as in Figure 8) is shown, but in Figure 9c, the point values are also included. The thick line in Figures 9a and 9b shows the average velocity for the whole 6 h interval.

vectors in Figures 5 and 6. Due to the downdrafts, the average vertical velocity profiles from the plumes are different from the velocity profiles in Figure 4, many of which are associated with turrets that remain identifiable due to the fact that they rise faster than the surrounding plume. Clearly, the average vertical velocities with the Eulerian method (Figure 8) are in all cases far lower than those obtained with the Lagrangian method (Figure 4).

[37] In Figure 6d the plume velocities could only be estimated for two sections of the plume, with one extending from the vent to the upper part. The lower section had predominantly lateral motion and low vertical velocity, whereas the other section showed strong vertical motions at low levels. Figure 8d shows, in blue, the average profile

obtained for both sections, and, in red, the profile obtained for the section of the plume that extends from the vent to the upper part. Obviously, when the low velocities below 2500 m are excluded, the profile shows higher velocities at low levels.

4.3. Are Average Vertical Velocity Profiles Representative?

[38] The vertical velocity profiles obtained with the Lagrangian and Eulerian methods (Figures 4 and 8) differ not only in the magnitude, but the shape of the profiles is also substantially different. The obvious question is, whether the averaging time in Figure 8 is long enough to yield representative averages for the plume motion, i.e., profiles that do

not change radically between sequential averaging periods. In the analysis of *Petersen et al.* [2012], individual starting plumes during the Eyjafjallajökull eruption took 2–4 min rising from the vent to the top of the plume, a time interval similar to that of the four cases in Figure 8. However, given the pulsating nature of the plume motion (Figure 7), it is possible that this time interval is too short for stable profiles. Indeed, it is about half that suggested by *Sparks et al.* [1997] for steady state model to apply, but within the range suggested by *Scase* [2009] for time-dependent plume models. In the latter study it was suggested to use as a “rule of thumb” that if the material properties within the cloud at any given moment cannot be associated with the current conditions at the vent, then a time-dependent model is appropriate. If, however, changes in the eruption are slow enough, then steady state models are appropriate, and the velocity profiles should change slowly, driven by changes in conditions at the vent.

[39] To examine this, velocities on 17 April were mapped for the time period starting at 15:00 UTC extending to 21:00 UTC. The average vertical velocities were calculated in the same manner as was done in Figures 8a and 8b. Figure 9 shows the results of calculating the average vertical velocities for all 5, 10, and 30 min intervals. For visualization, only the results of applying a loess smoothing filter to the data are shown in Figures 9a and 9b while the individual average data points are also shown in Figure 9c. The average velocity profile for the whole interval is shown as a thick line in Figures 9a and 9b.

[40] The spaghetti diagram in Figure 9a clearly shows that the 5 min average profiles are usually not stable in that there often are large differences between sequential profiles. One can, however, also see cases where profiles that are closely spaced in time show very similar shape, probably reflecting time intervals when the conditions at the source remained steady for periods longer than 5 min. Examination of the 10 min profiles also shows many instances where the profile radically changes shape from one 10 min interval to another. However, the 10 min profiles (Figure 9b) also show velocities above 3 km altitude gradually changing throughout the sequence. Early on, these velocities tend to be higher than the average velocity for the 6 h interval, but in the latter part of the time interval, vertical velocities above 3 km are less than the average. The 30 min profiles (Figure 9c) show a similar progression and range of velocities as the 10 min profiles. On average, the velocity profiles for the 6 h interval show a speedup with altitude below 3 km and a slowdown above.

[41] If the velocity profiles observed on the exterior of the plume for the 6 h period could be represented with a steady profile (see black lines in Figures 9a and 9b) plus high-frequency stochastic variations, the width of the profile envelope should be reduced for the longer averaging periods. This is examined in Figure 9d, which shows the interquartile range of the velocity estimates as a function of altitude for the three averaging periods. The figure shows that between 2 and 4 km, the width of the envelope of 30 min averages is close to 1 m s^{-1} , whereas it is $1.5\text{--}2 \text{ m s}^{-1}$ for the 5 min averages. Above 4 km the three averaging periods yield envelopes of similar width. Thus, the width of the envelope is reduced with increased averaging at lower levels but not above 4 km. The fact that the velocity estimates

are not consistently narrower is further evidence that the velocity profiles are not stable.

5. Discussion

[42] In the standard model for a volcanic plume, most of the vertical extent of the plume results from buoyancy driven convection. Atmospheric and source conditions define how much the plume rises, and how the vertical velocity changes with height. Modeling shows that usually the velocity will decrease with height above the momentum driven gas thrust region, but if the eruption is strong enough, a super-buoyant velocity profile may occur, in which velocities increase with altitude in the lower part of the convective region.

[43] As discussed in section 1, there is limited empirical evidence from volcanic eruptions regarding the velocity structure of volcanic plumes. Three questions were identified relating to the spatial and temporal variability of the velocity within the plume, and how representative the starting plume velocity estimates are of the plume velocities in general. Here the velocity structure on the plume exterior during the 2010 Eyjafjallajökull eruption has been mapped and its spatial and temporal variations examined for four time intervals covering all three phases of the eruption. On the basis of this analysis it is now possible to address these questions.

[44] First, mapping of the spatial distribution of plume velocities shows that upward motion prevailed throughout part of the plume giving way to lateral or even downward motion downwind from the vent. Second, even in the updraft part of the plume, the updraft was not continuous, but alternated between strong updrafts, weak upward motion, and downdrafts, similar to atmospheric convection clouds. Third, the average vertical velocities differed considerably from those of fast rising turrets. The average vertical velocities ranged from 5 to 10 m s^{-1} , but analysis of the fast rising turrets yielded velocities of up to 25 m s^{-1} during the explosive phases, with lower velocities in the effusive phase. The two different kinds of vertical velocity estimates did not yield a similar profile, and indeed, during a 6 h period, the average vertical velocity profile varied significantly, even for a 30 min average.

[45] The conceptual picture that these results suggest is different from the one underlying the integral plume models discussed in section 1. Instead of a steady or slowly varying source, giving rise to a plume with a well-defined vertical velocity profile, the results rather suggest a plume driven by intermittent explosions of varying strength, followed by strong updrafts and fast rising cloud turrets. For the dynamics of the plume and the lofting of ash, the updrafts and turrets are of considerable importance.

[46] In the buoyant phase, the rise velocities of starting plumes can, on theoretical grounds, be expected to be lower than the plume average. The reason is that the starting plume will need to entrain stationary ambient air and thus expends some of its momentum on accelerating it. Indeed, *Turner* [1962] found empirically that the starting plume moved at about 60% of the mean velocity on the axis of a steady plume. However, *Scase* [2009] points out that these were based on experiments with water and brine, and may not be generalizable to volcanic plumes. The Lagrangian tracking in this study follows identifiable turrets on the edge of

the volcanic cloud, and, as stated in section 1, this might be considered analogous to starting plumes originating in an explosion at the vent.

[47] However, identifying the rising turrets as starting plumes is problematic, since the analysis herein shows that they rise faster than the surrounding medium, not slower as theory would have it. Indeed, the pulsating nature of the plume revealed in Figure 7 seems to indicate that the rising part of the plume consists of individual thermals, rising fast through a background with slower ascending vertical motion, and with downward motion in the wake of the thermals. Note that as the method can only see motion on the exterior of the plume, it is, in principle, possible that the plume consists of a fairly steady core with transient vortices on the edges. However, such a description would conflict with the findings of *Ripepe et al.* [2013] who found, using infrasound and thermal images, that the plume was intermittent in behavior and described it as “continuous occurrence of puffs”. Furthermore, *Bonadonna et al.* [2011] also noted pulsations in the plume, and that ash injection into the atmosphere was variable. A steady core with transient vortices thus appears less likely as an explanation for the pulsation seen in Figure 7 than a sequence of thermals.

[48] The average vertical velocity profiles exhibit a substantial amount of variability, even within the same day (Figure 9). In general, though, they show a speedup in the lower part of the plume. It is unclear if this speedup in the convective part of the plume is the super-buoyant behavior described by *Bursik and Woods* [1991], but the results herein also show that downwind from the vent the average motion of the plume can be downward, most likely associated with fallout from the plume.

[49] The theory of thermally buoyant plumes is set up in a framework of a continuous well-defined plume. The results herein show that the velocity structure is characterized by individual explosive events, and this suggests that elementary parcel theory [*Rogers and Yau*, 1989] may help elucidate certain aspects of the plume behavior. According to this theory, a parcel subject to positive buoyancy will accelerate vertically; how much is influenced by the strength of the buoyancy source, the mass burden (the weight of particulate matter) of the parcel, and momentum exchange with the surroundings. Here fallout from the plume is likely to alter substantially the mass burden which then alters the dynamics. It is possible that the “super-buoyancy like” behavior seen here owes more to the interactions of buoyancy dynamics and changes in mass loading than the standard *Bursik and Woods* [1991] theory. However, this agrees with the results of *Woods and Bursik* [1994] who examined the influence of particle fallout on the formation of a buoyant plume in a laboratory setting and found that sedimentation exerted a strong influence on the buoyancy generation.

[50] Parcel theory also has a bearing on particle size and fallout. In general, fallout from a cloud will occur when the updraft is not sufficiently strong to keep particles suspended [*Rogers and Yau*, 1989]. This occurs when the terminal fall speed of the particles is greater than the updraft speed. The pulses of strong updrafts seen in Figure 7, for the three phases of the eruption, are therefore chiefly responsible for lofting ash higher up into the atmosphere. As a consequence, these are the velocities that matter with regard to ash transport into the umbrella cloud, not the average plume

velocities. As terminal velocities are related to particle size, it follows that in cases where the velocity decreases with altitude, the size distribution within the plume is automatically differentiated with only the smallest particles staying suspended in the upper part of the cloud where the updraft is weakest.

[51] It should be noted that the results above are not without caveats. The velocities estimated herein are based on visual characteristics on the exterior of the plume. It is possible that within the plume, higher velocities existed, unseen by the analysis method employed here. Indeed, higher velocities that have no expression on the exterior of the plume would be invisible to this method. However, as we have noted, the plume was characterized by pulsations, and high velocity thermals of long enough duration would overtake slower obscuring thermals and become visible at the top of the plume. Furthermore, the eruption of Eyjafjallajökull had three different phases, and although results of each of these phases have been presented here, they only cover the cases of a weak and a moderate eruption. Thus, it is not clear if these results can be generalized to stronger eruptions.

[52] To summarize, the results herein indicate high degree of spatial and temporal variability within the plume, both the pulsating nature and fallout from the plume lead to characteristics different from those expected from standard integral plume models.

Appendix A: Methodological Details

A1. Calculation of the Correlation

[53] Tracking an identifiable feature with the MCC method requires repeated calculation of correlation. If the target box enclosing the feature (see Figure 2a) has dimensions of n by n pixels, and encompassing it we define a “search-box” that extends p pixels surrounding the target box as shown in Figure A1, the number of correlations that must be calculated is given by

$$(p+n+p+1-n)(p+n+p+1-n) = (2p+1)^2.$$

The MCC is then taken as the largest of the $(2p+1)^2$ correlation values calculated.

[54] It is interesting to note that the number of correlations that must be calculated is not dependent on the dimensions of the target box but only the size of the surrounding region (p pixels in this example). However, the number of *arithmetic operations* needed for the calculation of *each* correlation is dependent on the number of pixels in the target box.

[55] The direct way of calculating the correlation is to simply step through all possible $(2p+1)^2$ configurations of the target box within the search box, calculate the correlation, and save the maximum value. As pointed out by *Clark et al.* [1968], Fourier transforms allow for the efficient calculation of correlations, as it involves a convolution operation, which may be efficiently calculated via direct multiplication of the Fourier transformed image in the search box and in the target. The number of operations in the direct calculation of the convolution increases proportional to $p^2 \times n^2$ whereas by using the Fourier transformed method, the increase is proportional to $p^2 \times \log_2(p)$. When p is much larger than n , the direct method is faster than the transform method, but the latter method becomes more efficient as p approaches n , especially for large n, p [*Lewis*, 1995]. In the

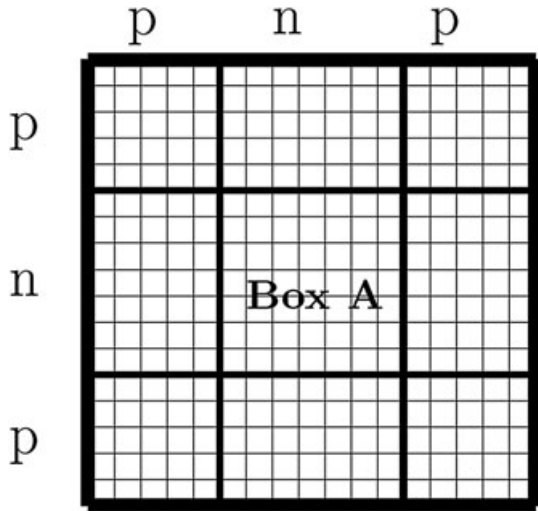


Figure A1. A target box A with dimensions n by n pixels, and a search box that extends p pixels surrounding Box A . An examination of the figure should easily reveal that the number of ways box A can be positioned within the search box is $(2p + 1)^2$.

supporting information, the MCC method is implemented for the tracking of identifiable features using two different MATLAB™ packages, one using the `normxcorr2` function which belongs to the Image Processing Toolbox™ and also using the `normxcorrn` function which belongs to Piotr's Image & Video MATLAB Toolbox [Dollár, 2012]. For the grid calculations, only the latter toolbox is used as it is free and easily available. The authors of both functions have added functionality to automatically decide at computation time whether to use direct calculation of the convolution or the transform method. Thus, the MCC method as implemented in the supporting information is sufficiently flexible to be used for different choices of p and n .

A2. Details on the Lagrangian and Eulerian Frameworks

[56] For the Lagrangian tracking of identifiable features, a portion of the cloud is selected and tracked through the sequence of images. It was found that the results obtained were more robust when the sequence was run backward, i.e., the identifiable features were selected toward the end of the image sequence, and then traced back toward the source at the vent. By running the method backward in time, it was easier to pick features that remained distinct throughout their rise in the plume. Each track yields time series of position in the plume, and vertical (and lateral) velocities were calculated using centered differencing.

[57] Several experiments were conducted to choose appropriate values for n , the size of the target box and p which determines the size of the search box (see Figure A1). The larger the target box, the less sensitive the method is to details of the cloud motion, but too small a box and the method yields tracks that jump around erratically, resulting in trajectories that are not robust in the sense that nearby starting points may diverge, leading to a scatter in velocity estimates. Experimentation showed that $n = 21$ provided a good balance between detail and robust tracks.

[58] The size of the search box needs to be big enough so that a features tracked do not move out of the search box between images. However, as the number of operations needed in the MCC method depends strongly on the size of the search region, p should be chosen as small as possible. A visual inspection of many image sequences showed that features were translated mostly by about 17 pixels between successive images, and on the basis of that, $p = 20$ was chosen. These values for n and p proved to be adequate and were used for both the Lagrangian and Eulerian methods. Using these numbers for n and p , both `normxcorr2` and `normxcorrn` use the direct method for calculating the MCC rather than the transform methods.

[59] When the MCC method was applied on a grid, care had to be taken with stationary and near stationary features, such as topography and distant clouds. As these features do not move, they have high correlation at zero translation. To avoid artifacts due to this, the MCC method was applied to the first order difference sequence. In other words, rather than tracking features from image 1 to image 2, features were tracked from image D1 to image D2 where D1 was the difference between images 2 and 1, and image D2 was the difference between images 3 and 2 (and so on for subsequent images). The first order differencing works as a simple moving-edge detector and resulted in a cleaner plume detection (see Figure 3).

[60] **Acknowledgments.** During this project, S. M. was supported by the Icelandic Student Innovation Fund, and this work was further supported by the FP7 Futurevolc project. During part of this work, H. B. was on a sabbatical at the Department of Atmospheric and Oceanic Sciences at McGill University. We are grateful to Maurizio Ripepe and two anonymous reviewers whose insightful comments improved this paper.

References

- Araon, P., G. N. Petersen, and H. Bjornsson (2011), Observations of the altitude of the volcanic plume during the eruption of Eyjafjallajökull, April–May 2010, *Earth Syst. Sci. Data*, 3, 9–17, doi:10.5194/essd-3-9-2011.
- Arking, A., R. C. Lo, and A. Rosenfield (1978), A Fourier approach to cloud motion estimation, *J. Appl. Meteorology*, 17, 735–744.
- Bonadonna, C., R. Genco, M. Gouhier, M. Pistolesi, R. Cioni, F. Alfano, A. Hoskuldsson, and M. Ripepe (2011), Tephra sedimentation during the 2010 Eyjafjallajökull eruption (Iceland) from deposit, radar, and satellite observations, *J. Geophys. Res.*, 116, B12202, doi:10.1029/2011JB008462.
- Briggs, G. A. (1969), *Plume Rise, US Atomic Energy Commission, Critical Review Series*, 81 pp., Oaks Ridge National Laboratory, Oaks Ridge.
- Bursik, M. (2001), Effect of wind on the rise height of volcanic plumes, *Geophys. Res. Lett.*, 28, 3621–3624, doi:10.1029/2001GL013393.
- Bursik, M., and A. W. Woods (1991), Buoyant, superbuoyant and collapsing eruption columns, *J. Volcanol. Geotherm. Res.*, 45, 347–350, doi:10.1016/0377-0273(91)90069-C.
- Carazzo, G., E. Kaminski, and S. Tait (2008), On the rise of turbulent plumes: Quantitative effects of variable entrainment for submarine hydrothermal vents, terrestrial and extra terrestrial explosive volcanism, *J. Geophys. Res.*, 113, B09201, doi:10.1029/2007JB005458.
- Carey, S., and R. S. J. Sparks (1986), Quantitative models of the fallout and dispersal of tephra from volcanic eruption columns, *Bull. Volcanol.*, 48, 109–125.
- Clark, B. B., J. A. Leese, R. L. Stallard, and P. Wrotenbe (1968), Cross-correlation using fast Fourier transform to obtain cloud motion from ATS cloud photographs, *Bull. Am. Meteor. Soc.*, 49, 1032–1042.
- Dacre, H. F., et al. (2011), Evaluating the structure and magnitude of the ash plume during the initial phase of the 2010 Eyjafjallajökull eruption using lidar observations and NAME simulations, *J. Geophys. Res.*, 116, D00U03, doi:10.1029/2011JD015608.
- Degruyter, W., and C. Bonadonna (2012), Improving on mass flow rate estimates of volcanic eruptions, *Geophys. Res. Lett.*, 39, L16308, doi:10.1029/2012GL052566.
- Dollár, P. (2012), *Piotr's Image and Video MATLAB Toolbox (PMT)*. <http://vision.ucsd.edu/~pdollar/toolbox/doc/index.html>.

- Giri, R. K., and R. K. Sharma (2011), FFT and MCC algorithms comparison in the identification of tracers for atmospheric motion estimation, *Int. J. Sci. Emerging Tech.*, *2*, 42–52.
- Glaze, L. S., and S. M. Baloga (1996), The sensitivity of buoyant plume heights to ambient atmospheric conditions: Implications for volcanic eruptions, *J. Geophys. Res.*, *101*, 1529–1540, doi:10.1029/95JD03071.
- Gudmundsson, M. T., et al. (2012), Ash generation and distribution from the April–May 2010 eruption of Eyjafjallajökull, Iceland, *Sci. Rep.*, *2*, 1–12, doi:10.1038/srep00572.
- Harris, A. J. L., M. Ripepe, and E. A. Hughes (2012), Detailed analysis of particle launch velocities, size distributions and gas densities during normal explosions at Stromboli, *J. Volcanology and Geothermal Res.*, *231*, 109–131, doi:10.1016/j.jvolgeores.2012.02.012.
- Lavergne, T., S. Eastwood, Z. Teffah, H. Schyberg, and L. A. Breivik (2010), Sea ice motion from low resolution satellite sensors: An alternative method and its validation in the Arctic, *J. Geophys. Res.*, *115*, C10032, doi:10.1029/2009JC005958.
- Leese, J. A., C. S. Novak, and B. B. Clark (1971), An automated technique for obtaining cloud motion from geosynchronous satellite data using cross correlation, *J. Appl. Meteorology*, *10*, 110–132.
- Lewis, J. P. (1995), Fast template matching, *Vision Res.*, *95*, 120–123.
- Mastin, L. G. (2007), A user-friendly one-dimensional model for wet volcanic plumes, *Geochem. Geophys. Geosyst.*, *8*, Q03014, doi:10.1029/2006GC001455.
- Mastin, L. G., et al. (2009), A multidisciplinary effort to assign realistic source parameters to models of volcanic ash-cloud transport and dispersion during eruptions, *J. Volcanol. Geotherm. Res.*, *186*, 10–21, doi:10.1016/j.jvolgeores.2009.01.008.
- Morton, B. R., G. Taylor, and J. S. Turner (1956), Turbulent gravitational convection from maintained and instantaneous sources, *Proc. R. Soc. Lond. A*, *234*, 1–23, doi:10.1098/rspa.1956.0011.
- Petersen, G. N., H. Bjornsson, and P. Arason (2012), The impact of the atmosphere on the Eyjafjallajökull 2010 eruption plume, *J. Geophys. Res.*, *117*, D00U07, doi:10.1029/2011JD016762.
- Ripepe, M., C. Bonadonna, A. Folch, D. Delle Donne, G. Lacanna, E. Marchetti, and A. Höskuldsson (2013), Ash-plume dynamics and eruption source parameters by infrasound and thermal imagery: The 2010 Eyjafjallajökull eruption, *Earth Planet. Sci. Lett.*, *366*, 112, doi:10.1016/j.epsl.2013.02.005.
- Rogers, R. R., and M. K. Yau (1989), *A Short Course in Cloud Physics*, 3rd ed., 113 pp., ISBN 978-0750632157, Pergamon Pres, Butterworth-Heinemann.
- Sahetapy-Engel, S. T., and A. J. L. Harris (2009), Thermal-image-derived dynamics of vertical ash plumes at Santiaguito volcano, Guatemala, *Bull. Volcanol.*, *71*, 827–830, doi:10.1007/s00445-009-0284-8.
- Scase, M. M., C. P. Caulfield, S. B. Dalziel, and J. C. R. Hunt (2006), Time-dependent plumes and jets with decreasing source strengths, *J. Fluid Mech.*, *563*, 443–462.
- Scase, M. M. (2009), Evolution of volcanic eruption columns, *J. Geophys. Res.*, *114*, F4003, doi:10.1029/2009JF001300.
- Settle, M. (1978), Volcanic eruption clouds and the thermal power output of explosive eruptions, *J. Volcanol. Geotherm. Res.*, *3*, 309–324, doi:10.1016/0377-0273(78)90041-0.
- Sigurðeirsson, T. (1966), Jarðdælisfræðirannsóknir í sambandi við Surtseyjargosid (Geophysical research in connection with the volcanic eruption at Surtsey) [in Icelandic with English summary], *Náttúrufræðingurinn*, *35*(4), 188–210.
- Sparks, R. S. J., M. I. Bursik, S. N. Carey, J. S. Gilbert, L. S. Glaze, H. Sigurdsson, and A. W. Woods (1997), *Volcanic Plumes*, ISBN 0471939013, 1st ed., 574 pp., John Wiley, Chichester.
- Sparks, R. S. J. (1986), The dimensions and dynamics of volcanic eruption columns, *Bull. Volcanol.*, *48*, 3–15, doi:10.1007/BF01073509.
- Sparks, R. S. J., and L. Wilson (1982), Explosive volcanic eruptions—V. Observations of plume dynamics during the 1979 Soufriere Eruption, St. Vincent, *Geophys. J. Roy. Astron. Soc.*, *69*(2), 551–570.
- Turner, J. S. (1973), *Buoyancy Effects in Fluids*, 368 pp., ISBN 052108623, Cambridge Univ. Press, Cambridge.
- Turner, J. S. (1962), The “starting plume” in neutral surroundings, *J. Fluid Mech.*, *13*, 356–368.
- Tupper, A., C. Textor, M. Herzog, H.-F. Graf, and M. S. Richards (2009), Tall clouds from small eruptions: The sensitivity of eruption height and fine ash content to tropospheric instability, *Nat. Hazards*, *51*, 375–401, doi:10.1007/s11069-009-9433-9.
- Velden, C., J. Daniels, D. Stettner, D. Santek, J. Key, J. Dunion, K. Holmlund, G. Dengel, W. Bresky, and P. Menzel (2005), Recent innovations in deriving tropospheric winds from meteorological satellites, *Bull. Amer. Meteor. Soc.*, *86*, 205–223, doi:10.1175/BAMS-86-2-205.
- Wilson, L. (1976), Explosive volcanic eruptions—III. Plinian eruption columns, *Geophys. J. Roy. Astron. Soc.*, *45*, 543–556, doi:10.1111/j.1365-246X.1976.tb06909.x.
- Wilson, L., R. S. J. Sparks, T. C. Huang, and N. D. Watkins (1978), The control of volcanic column heights by eruption energetics and dynamics, *J. Geophys. Res.*, *83*(B4), 1829–1836, doi:10.1029/JB083iB04p01829.
- Wilson, L., R. S. J. Sparks, T. C. Huang, and N. D. Watkins (1987), Explosive volcanic eruptions—VI. Ejecta dispersal in plinian eruptions: The control of eruption conditions and atmospheric properties, *Geophys. J. Roy. Astron. Soc.*, *89*, 657–679, doi:10.1111/j.1365-246X.1987.tb05186.x.
- Woodhouse, M. J., A. J. Hogg, J. C. Phillips, and R. S. J. Sparks (2013), Interaction between volcanic plumes and wind during the 2010 Eyjafjallajökull eruption, Iceland, *J. Geophys. Res. Solid Earth*, *118*, 92–109, doi:10.1029/2012JB009592.
- Woods, A. W. (1988), The fluid dynamics and thermodynamics of eruption columns, *Bull. Volcanol.*, *50*, 169–193, doi:10.1007/BF01079681.
- Woods, A. W., and M. I. Bursik (1994), A laboratory study of ash flows, *J. Geophys. Res.*, *99*(B3), 4375–4394, doi:10.1029/93JB02224.
- Yahia, H., J. Sudre, C. Pottier, and V. Garçon (2010), Motion analysis in oceanographic satellite images using multiscale methods and the energy cascade, *Pattern Recognit.*, *43*, 3591–3604, doi:10.1016/j.patcog.2010.04.011.